Near-Fault Broadband Ground Motion Simulations Using Empirical Green's Functions: Application to the Upper Rhine Graben (France–Germany) Case Study

Sergio del Gaudio, Sébastien Hok, Gaetano Festa, Mathieu Causse, Maria Lancieri

Near fault broadband ground motion simulations using empirical Green's functions: application to the Upper Rhine Graben (France-Germany) case study.

Sergio Del Gaudio*, Sebastien Hok*, Gaetano Festa*, Mathieu Causse** and Maria Lancieri***

** IRSN – Institut de Radioprotection et de Sûreté Nucléaire*

IRSN/PRP-DGE/SCAN/BERSSIN

31, avenue de la Division Leclerc - 92262 Fontenay-aux-Roses Cedex, Bât. FAHRENHEIT pièce 721

sergio.delgaudio@irsn.fr

*** Université de Grenoble Joseph Fourier, Institut des Sciences de la Terre (ISTerre)*

**** Department of Physics, Università di Napoli Federico II*

Abstract

Seismic hazard estimation relies classically on data based ground motion prediction equations (GMPEs) giving the expected motion level as a function of several parameters characterizing the source and the sites of interest. However, records of moderate to large earthquakes at short distances from the faults are still rare. For this reason, it is difficult to obtain a reliable ground motion prediction for such a class of events and distances where also the largest amount of damage is usually observed. A possible strategy to fill this lack of information is to generate synthetic accelerograms based on an accurate modeling of both extended fault rupture and wave propagation process.

The development of such modelling strategies is essential for estimating seismic hazard close to faults in moderate seismic activity zones, where data are even scarcer. For that we reason we selected a target site in Upper Rhine Graben (URG), at the French-German border. URG is a region where faults producing micro-seismic activity are very close to the sites of interest (e.g. critical infrastructures like supply lines, nuclear power plants, etc.) needing a careful investigation of seismic hazard.

In this work we demonstrate the feasibility of performing near-fault broadband ground motion numerical simulations in a moderate seismic activity region such as Upper Rhine Graben (URG) and discuss some of the challenges related to such an application. The modelling strategy is to couple the multi-Empirical Green's Function technique (multi-EGFt) with a k^{-2} kinematic source model. One of the advantages of the multi-EGFt is that it does not require a detailed knowledge of the propagation medium since the records of small events are used as the medium transfer function, if, at the target site, records of small earthquakes located on the target fault are available.

The selection of suitable events to be used as multi-EGF is detailed and discussed in our specific situation where little number of events are available. We then showed the impact that each source parameter characterizing the k^{-2} model has on ground motion amplitude. Finally we performed ground motion simulations showing results for different probable earthquake scenarios in the URG.

Dependency of ground motions and of their variability are analyzed at different frequencies in respect of rupture velocity, roughness degree of slip distribution (stress drop), and hypocenter location. In near source conditions, ground motion variability is shown to be mostly governed by the uncertainty on source parameters. In our specific configuration (magnitude, distance), the directivity effect is only observed in a limited frequency range. Rather, broad-band ground motions are shown to be sensitive to both average rupture velocity and its possible variability, and to slip roughness. Ending up with a comparison of simulation results and GMPEs, we conclude that source parameters and their variability should be set up carefully in order to obtain reliable broadband ground motion estimations. In particular, our study shows that slip roughness should be set up in respect to the target stress drop. This entails the need for a better understanding of the physics of earthquake source and its incorporation in the ground motion modelling.

Introduction

To estimate the seismic hazard assessment (SHA), a proper modeling of the ground motion is a fundamental step. This is commonly done through the use of ground motion prediction equations (GMPEs), which are empirical relations obtained by the regression of recorded data and metadata. The GMPEs estimate the ground motion level as a function of several parameters

concerning either the source, the wave path and the site such as distance, magnitude, fault type, soil conditions, etc. The increase of the number and quality of strong motion records associated to moderate to large earthquakes worldwide led to a significant improvement in the GMPEs (Douglas and Edwards 2016). A variety of GMPEs has been proposed for several engineering parameters (PGA, spectral ordinates, PGV, Intensity measurement) accounting for different source mechanisms, tectonic environment, geographical areas and specific sites effects (e.g. Campbell and Bozorgnia, 2014). A comprehensive collection of GMPEs can be found in Douglas (2016). GMPEs are widely used because they are computationally inexpensive and they have associated uncertainties that can be integrated in the hazard evaluation.

Nevertheless, GMPEs do not represent the variety of source and propagation, indeed the source is mainly described by the magnitude and, for the recent GMPEs, also by the fault geometry and focal mechanism, but the rupture process is not taken into account. In addition, one could question of the confidence we can have in the extrapolation beyond their range of validity. This is especially true in near fault conditions and for large crustal events, where the scarcity of available data can lead to incorrect estimates when applied to some specific case studies (Boore, 2001). These specific cases include for example, interaction between the earthquake rupture and basins (Koketsu and Miyake, 2008) or surface rupture for normal or thrust faults (Donahue and Abrahamson, 2014) and all the cases where the time history content is dominated by the source characteristics (e.g. see example of Tocopilla earthquake studied by Lancieri et al., 2012). In such cases, ground motion simulations will likely be a better modelling than GMPEs, provided that both source and propagation are accurately described and uncertainties properly addressed. Moreover, we simulate complete waveforms having amplitudes and phases information, while GMPEs only gives us information about the amplitude of the ground motion.

The knowledge of the seismic source is generally based on different parameters: some of them can be investigated or inferred from local geology (e.g. position and geometry of the faults), or

geophysical studies (e.g. the depth of the faults); other parameters, related to the kinematic and dynamic properties of the source, can be either assumed *a priori* making some hypothesis (e.g. magnitude of the event we want to simulate) or chosen from a range of possible values. This latter strategy leads to different resulting scenarios by defining an a priori probability distribution for each parameter: e.g. rupture velocity, slip distribution, hypocenter position on the fault plane, etc. In this paper, we will show how to produce a population of ground motion records representing the possible variability of the source process for a target earthquake (e.g. Causse et al. 2008; Cultrera et al. 2010).

When the target scenario refers to historical or paleoseismic events, and no instrumental record is available, the ground motion simulations are referred to as "blind". Performing blind simulations is helpful not only to deduce an expected ground motion level, but its variability as well.

We can separate this variability in two different parts: the aleatory and the epistemic contributions. The aleatory part cannot be reduced because it comes from features that are essentially or apparently random in nature. The aleatory variability comes from any parameter that is intrinsically variable during the rupture process. The epistemic part though, since it is related to the variable modelling strategy and parameterization can be potentially reduced investigating the physics and improving our knowledge of the rupture process. For instance, physics-based rupture models showed correlations between different kinematic source parameters and the influence that they have on the ground motion (Song et al., 2014; Schmedes et al., 2010).

Simulations of ground motions accounting for source variability can be performed through the use of numerical codes that couple the source dynamics or kinematics with the complete wavefield propagation in 3D complex media. Several techniques are commonly used to provide reliable ground motion accelerograms, such as the Spectral Element Method (e.g. Komatitcsh

et al., 2004; Cupillard et al., 2012), the Finite Differences method (e.g. Day et al., 2005; Dalguer and Day, 2007; Aochi et al., 2011) and the Discontinuous Galerkin Method (e.g. Dumbser and Kaeser 2007; Mazzieri et al., 2013). Accuracy in the strong motion modelling depends on the knowledge of the structure, which is, in the best cases, limited at space scales larger than hundreds of meters. The main problem of these approaches is that for many sites crustal models are barely known. In addition, for broadband ground motion estimations (above 10Hz) those numerical schemes need to be completed by stochastic high frequency methods.

For these reasons, the use of Empirical Green's Functions (EGF) may help in correctly model the wave propagation up to short wavelengths (Hartzell, 1978; Irikura, 1983), providing an elastic response of the medium and a compatibility of the small earthquakes with the target event to simulate in terms of location on the fault, focal mechanism and stress drop (Irikura, 1984). Although this approach was developed and validated for far-field broadband simulations, it has been recently extended by Del Gaudio et al. (2015) to the near fault case through the introduction of the multi-EGF concept. In this concept, different EGFs are attributed to different part of the target fault in order to cover the whole range of different orientations between the source and a receiver that is close to it, so that the approximation of EGF remains valid locally. Regarding the source process, the multi-EGF technique is coupled with a k^{-2} kinematic model (Herrero and Bernard, 1996) that will be described in the methodology section of the paper. This methodology allows for rapid estimations of broadband ground motions in the near fault area together with a detailed extended source description, without needing either a detailed knowledge of propagation medium nor additional methodologies for modeling different frequency bands. This methodology of broadband ground motion simulations is thus adapted to the need for challenging GMPEs on their limited range of validity close to faults, especially due to their lack of precision regarding source description.

Finally, we face an additional challenge regarding SHA and GMPEs in moderate to low seismic activity context. In such areas, small earthquakes are recorded and estimation of seismic hazard is needed. However, GMPEs are criticizable in such places because of the possible inconsistency between the local context and the data used in the GMPE. Therefore, simulations, and in particular EGFt, can improve the ground motion prediction. Thanks to the presence of multiple small earthquakes, EGFt can be applied directly to moderate seismicity areas. For that reason, we applied our methodology to the Upper Rhine Graben (URG) area, where minimal experimental conditions are found: active faults, recorded moderate seismicity, and need for a near-fault SHA. As a first step toward near-fault SHA, we perform broadband blind simulations for two scenarios (M_w 6 and M_w 6.5) on an active fault in the URG. Along the text we point out the difficulty in doing such an exercise in an area scarcely instrumented where information on small recorded events are imprecise.

After a description of the URG, we describe the implemented strategy to select and characterize the EGFs, to explore the source parameters variability and its influence on the resulting ground motion simulations.

We selected a target site which is located in very near fault conditions, but also close to seismic activity in the center of the Graben, where most of the infrastructures (e.g. buildings, roads, industries, etc.) and also some critical facilities (e.g. supply lines, nuclear power plants, etc.) are located.

1. Simulations method

1.1. Simulations method: EGF technique

Using the representation integral (Aki and Richards, 2002), the ground displacement recorded at a position $\bar{x}$ on the Earth's surface at a time t can be expressed as:

$$\boldsymbol{u}(\bar{x},t) = \int_{\Sigma} s_i(\bar{\xi},\tau) * \left[c_{ijkl}(\bar{\xi})\boldsymbol{\nu}_j(\bar{\xi})\boldsymbol{G}_{k,l}(\bar{x},\bar{\xi};t,\tau)\right] d\Sigma(\bar{\xi}) \quad (1)$$

where $\boldsymbol{s}$ is the slip vector, $\boldsymbol{c}$ is the elastic coefficient matrix, $\boldsymbol{\nu}$ is the normal to the fault, **G** is the Green's function and $\sum$ is the fault surface. Summation over repeated indices is assumed and the symbol * denotes time convolution. The Green's function represents the crustal medium response to an impulsive wave and it can be computed knowing the crustal structure (i.e. geometrical and rheological properties). In this work we adopted a simulation method based on the empirical Green's functions (EGF) approach. Many applications have made use of the EGFs for ground motion simulation (Hutchings 1994; Irikura & Kamae 1994; Hartzell et al. 1999; Causse et al. 2009; Del Gaudio et al. 2015) since the pioneering works of Hartzell (1978) and Irikura (1986). This technique consists in replacing the contribution $c_{ijkl}(\bar{\xi})\boldsymbol{\nu}_j(\bar{\xi})\boldsymbol{G}_{k,l}(\bar{x},\bar{\xi};t,\tau)$ with the displacement record of a small earthquake $\boldsymbol{G_e}(\bar{x},\bar{\xi})$ having the same location as the Green function, sharing the same focal mechanism and stress drop as the target event. After multiplication by the shear modulus μ and normalization by the seismic moment of the small event $M_{\bar{G}}$, we obtain:

$$\boldsymbol{u}(\bar{x},t) = \int_{\Sigma} \frac{\mu}{M_{\bar{G}}} S(\bar{\xi};\tau) * \boldsymbol{G}_e(\bar{x},\bar{\xi};\tau)\, d\Sigma(\bar{\xi}) \quad (2)$$

The record of small earthquake used to describe the medium response is generally referred to as an EGF. The index *i* of the slip function has been removed because we assumed a constant rake direction, so *S* now only represents the amplitude of the slip.

For broadband simulations, the main advantage of using EGFs is that we do not need a detailed knowledge of the crustal velocity structure; we indeed need a good quality location catalog of small events and some reliable indication of the fault geometry, moreover the earthquakes used as EGF should satisfy specific criteria: first of all, the signal-to-noise ratio has to be sufficiently large in all the frequency range of interest, its location and focal mechanism has to be

compatible with the fault plane considered for the target event and its magnitude must be at least 2 point smaller than the one of the target event.

Under this latter condition an EGF can be considered as the medium response to a Dirac delta function because it is a good approximation of a point source with respect to the large event to be simulated.

The space discretization on the fault plane is controlled by the size of the event used as EGF, according to earthquake scaling laws. Assuming self-similarity between the rupture of small and large events (Brune 1970), the number of subfaults associated to small events to be considered is

$$N = \frac{L}{l} = \frac{W}{w} = \left(\frac{M_0}{M_{\tilde{G}}} \right)^{1/3} \quad (3)$$

N is the spatial scale factor between the mainshock and the associated EGF. In this equation L, W and M_0 are the length, width, and seismic moment of the target event, respectively, while l, w and $M_{\tilde{G}}$ represent the same quantities for the small event. In this study we used squared subfaults with size $\Delta x = w$ to discretely solve equation (2).

1.2. Simulations method: the Multi-EGF approach

The classic EGF approach uses a single event as EGF translated along the fault plane. This is equivalent to assume that the propagation term (path, radiation) is the same for all the points of the crustal volume surrounding the fault plane. This is a strong approximation, especially for large faults and in near source conditions, where the wave path from fault to site varies strongly. To overcome this limit, Del Gaudio et al. (2015) proposed to use several EGFs, each EGF sampling the closest portion of the fault plane, allowing to better take into account the wave path and source radiation variability. This technique is called multi-EGF. Del Gaudio et al.

(2015) demonstrated the validity of the methodology on the 2009 L'Aquila earthquake using several aftershocks as multi-EGF to reproduce the main event accurately.

In practical, the difference with the single EGF technique is that the Green's function is variable along the fault plane. Each portion of the fault plane gets its own EGF as being the closest one, such as illustrated on Figure 1. In addition, a correction in time and amplitude is also applied to each EGF to take into account the difference between original hypocentral position of the event and applied subfault (see Causse et al. 2009). After a discretization of equation (2), the simulated displacement can be written as a summation of EGF

$$\boldsymbol{u}(\bar{x},t) = \sum_{ij} \frac{\mu^{(ij)}\Delta x^2}{M_{\bar{G}}^{(ij)}} S^{(ij)} * \boldsymbol{G}^{(ij)}(\bar{x},t) \qquad (4)$$

The indices *i* and *j* are related to subfault (*i*,*j*) and run over strike and dip directions respectively.

1.3. Simulations method: source model

To describe the source process we adopted the k^{-2} kinematic source model (Herrero and Bernard, 1996; Gallovič and Brokešová, 2004). In the wavenumber domain **k**, this model is characterized by an asymptotic k^{-2} decay of the slip amplitude beyond the corner wavenumber $k_c = \aleph/L$, where L is the characteristic fault dimension and $\aleph$ is a non-dimensional parameter which represents the roughness degree of the slip distribution (in Figure S1 of the electronic supplement are shown two example of slip distributions for two different values of $\aleph$). This particular asymptotic behavior is able to reproduce the high frequency f^{-2} decay observed in far-field displacement spectra. While the slip amplitude spectrum in the wavenumber domain follows this model, the phase distribution φ is randomly chosen and it represents a source of variability for k^{-2} models. The slip distribution in the wavenumber domain can be summarized as

$$S_k(k_x, k_y) = \frac{\bar{S}LW}{\sqrt{1+\left[\left(\frac{k_x L}{\mathcal{K}}\right)^2+\left(\frac{k_y W}{\mathcal{K}}\right)^2\right]^2}} e^{i\varphi(k_x,k_y)} \quad (5)$$

where $\bar{S}$ is the average slip value, L, W, k_x and k_y are the fault dimensions and wavenumbers respectively along strike and dip directions.

Rise time is assumed to be *k*-dependent. In particular it is constant for $k < k_c$ and it linearly decreases with *k* for larger wavenumbers. Rupture velocity is assumed to be constant over the fault plane.

All the source parameters such as the roughness degree of the slip $\mathcal{K}$, the rupture velocity v_r, the rise time τ and the position of the hypocenter on the fault plane, can be deterministically defined (i.e. from a kinematic source model obtained from low frequency inversion) or randomly chosen from *a priori* distribution (Causse et al., 2009; Del Gaudio et al., 2015).

2. Upper Rhine Graben case study

To better investigate the advantages and limitation of the technique, and to test the influence that each considered source parameter has on the simulated ground motion and its variability, we set up an application to the Upper Rhine Graben (URG). The URG is a region located along the border line between French and Germany, characterized by a moderate level of seismicity.

Historically, one of the major West-European earthquakes happened in 1356, near Basel (Switzerland) at the Southern termination of the Graben. MKS maximum intensity of this event was estimated between VIII and IX (Mayer-Rosa and Cadiot, 1979), but the fault source has been not clearly identified (Mayer et al., 1994; Lambert et al., 2005; Meghraoui et al., 2001; Ferry et al., 2005).

The Rhine Graben is characterized by the presence of several fault systems. In Figure 2 all the segments that have shown evidence of activity are represented. Specifically we can recognize the Western Rhine Fault, at the western border of the Graben; the Black Forest Fault, at the eastern border of the Graben and the Rhine River Fault (Bertrand et al., 2006; Nivière at al., 2008; Palumbo et al., 2013), following the river path.

Considering historical seismicity and the large number of active faults in the area, people and infrastructures (e.g. buildings, roads, industries, etc.) and also some critical facilities (e.g. supply lines, nuclear power plants, etc.) are potentially exposed to the risk that comes from earthquakes generated along the URG. The size of the fault segments in the URG suggests that earthquakes with magnitude larger than 6 are likely to happen. Their return periods are estimated as a function of the magnitude (Nivière at al., 2008) and, for instance, a return interval of about 8000 years was estimated for the Rhine River Fault for an event of magnitude of 6.5.

In addition, such faults were also considered in long return period probabilistic seismic hazard assessment (PSHA) by Chartier (2015). Such studies use GMPEs to evaluate the ground motions close to the fault, where they are likely to be biased. As a consequence, ground motion simulations can provide a useful comparison with GMPEs and eventually an alternative choice for PSHA. For these reasons the URG is an interesting test case for applying our technique and performing blind ground motion simulations.

For the simulations, we decided to focus on the Rhine River fault. We considered this fault as divided in two segments. From surface evidence, we set their strikes equal to 172° for the northern segment, and 203° for the southern segment. From geological and geophysical investigations (Nivière at al., 2008) the faults are west dipping with an angle of approximately 60°-70°. We decided to adopt a dip angle of 70° but, for future applications, an exploration of different values should be performed in order to investigate the influence that it could have on

simulation results. Regarding the depth of the faults, we prolonged the surface trace up to a maximum depth of 15 km. In Figure 3 the two selected segments of the Rhine River Fault are schematically represented.

To perform ground motion simulation in the URG we faced several problems. Due to the fact that we are in "blind" conditions, kinematic parameters (e.g. rupture velocity, slip distribution) and dynamic parameters (e.g. stress drop, interaction between different fault segments) are unknown, as well as details regarding the fault geometry (e.g. hypocenter location, depth of the fault). Sensitivity studies for all the different parameters are, hence, required to characterize the aleatory and epistemic variability of the simulated ground motion. Moreover, the low rate of seismicity and the consequent small amount of records requires a careful investigation of the different events to be used as EGF, whose selection depends on the hypothesis for the target event (fault geometry, magnitude, etc.).

3. EGF Selection and Analysis

After selecting the fault geometry, we started screening data of small earthquakes to be used as an empirical approximation of the propagation medium response function. As described in the methodology section, to be used as an EGF, an event must satisfy specific criteria.

We screened out the French instrumental catalog Si-Hex (Sismicité instrumentale de l'Hexagone), the Renass (Réseau National de Surveillance Sismique) catalog, and the seismic catalog of the LGRB (Landesamt für Geologie, Rohstoffe und Bergbau) Institute of Freiburg in a time period ranging between January 2000 and December 2014. The seismological institutes responsible for the location of earthquakes indeed share the data across the border. Twenty-seven events were identified with a local magnitude ranging between 1.5 and 3.2 (Figure 3).

We decided to adopt the locations proposed by the LGRB catalog, because they are done without fixing the hypocentral depth. This choice will reduce possible biases in the correction for the geometrical spreading.

As target site we chose the BREM station (see Figure 3) which is close to both the considered faults (it's located exactly on the surface projection of both the faults planes and at about 5 km of geometrical distance from them).

We selected five events, three having the largest magnitude in the catalog, to have a large signal to noise ratio in a wide frequency range, and the two whose location is the closest to the selected fault system. In Figure 3, we plot all the considered events (black dots) and the selected EGF (red dots). From the figure results clear that two of the five selected EGF can be associated to the northern fault segment and three to the southern segment. Therefore our selection covers spatially the target faults, which is needed in the multi-EGF approach for near field computation. On the map the seismic stations located in the area belonging to both the French and the German national networks are also showed.

To verify the hypothesis of self-similarity of the EGF, we computed seismic moment and corner frequency and we inferred the apparent stress drop by inverting the S phase Fourier amplitude spectrum. The S wave has been manually picked on the records at the available stations. A time window of 5*s* (0.5*s* before and 4.5*s* after the S wave arrival time) containing the whole direct S-wave train has been isolated. We removed baseline from signals and computed displacement from acceleration by double integration. After computing Fourier spectra of the three components we combined them by vector summation. For the spectral inversion, we assumed in the angular frequency domain ω a ω^{-2} decay of the displacement spectrum beyond its corner frequency f_c (Brune, 1970). We also estimated the focal mechanisms for eligible EGF computing long-period spectral level ratios at each station (De Matteis et al., 2016). Because of the sparse network geometry, azimuthal gap (>300°), paucity of records and low signal to noise

ratio for P wave, we fixed the strike and the dip angle according to the geometry of the faults to which the event is related by proximity, and we computed the rake angle using single station spectral ratios between S and P displacement levels at low frequency. Assuming a Brune's source model, the ratio between the low frequency plateaus, can be expressed as:

$$\frac{\Omega_{0,s}}{\Omega_{0,p}} = \frac{R^{P}_{\lambda\varphi}}{R^{S}_{\lambda\varphi}}\left(\frac{v_s}{v_p}\right)^3 \quad (6)$$

where v_s and v_p are the mean values of P and S wave velocities and $R^{P,S}_{\lambda\varphi}$ are the radiation pattern coefficients which depend on the rake angle (a detailed formulation of this coefficients is given in Aki and Richards, 2002). After measuring the ratio, a grid search was performed to determine the value of the rake angle which at best approximates the equation (5). Two symmetric solutions are always available for the rake angle and, to remove this ambiguity, we have to measure P-wave polarities for each station. Obtained results show mainly a normal fault behavior with a strike slip component in the northern part, as showed also in previous studies performed for the same region (Homuth et al., 2014). For this reason, we did not apply any correction for the focal mechanism differences of the EGF.

Location and computed parameters of the selected EGFs are reported in TABLE 1. Figure 4 shows the retrieved corner frequency as a function of the seismic moment in a logarithmic scale respectively, for all the selected EGFs. In Figure S2 of supplementary material are also shown the spectral inversions for all the EGFs. As shown in Figure S2, not all the signals are characterized by a good signal to noise ratio in all the considered frequency range (from 1 to 20 Hz). In particular this ratio becomes lower than 1 at low frequencies for stations END, LIBD and STAU and EGF1, EGF3 and EGF4. We decided to keep these data and source parameters were obtained by making a weighted average of values computed for each station, with weights proportional to signal-to-noise ratios.

For the selected events, we found that the average stress drop ranges between 3*MPa* and 35 *MPa*. Nevertheless uncertainties are very large owing to the difficulty in well constraining the corner frequencies with a small number of records. Different values in the stress drop may lead to differences in simulated ground motion amplitude, increasing the epistemic variability associated with the EGFs. According to Del Gaudio et al. (2015), we applied a correction to each EGF. The EGF amplitude spectrums were first divided by their corresponding Brune spectrums, considering the seismic moment and stress drop values of TABLE 1. The spectra were next multiplied by a Brune spectrum associated to a reference seismic moment of a M_w 3 event with a stress drop $\Delta\sigma$=8 *MPa*, this latter value being the geometric mean of the EGF stress drops.

4. Ground motion simulations

4.1. Sensitivity analysis

We recall that, in blind conditions, we do not have a benchmark time history, so our aim is not to simulate an observed motion, but all the possible ground motions produced by all the possible source configurations. In fact, while the knowledge on fault geometry can be improved through geophysical investigations), dynamic and kinematic source parameters are unknown until the occurrence of a big earthquake. Moreover, they can be unique for each event and then, for this reason, it is necessary to make several simulations with variable source parameters to investigate all the possible scenarios and the variability associated to them.

The k^{-2} model is characterized by three parameters that mainly affect the ground motion: the roughness parameter $\mathcal{K}$ (eq. 4), the rupture velocity v_r and the nucleation position on the fault plane. We did sensitivity analysis for all of them. Figure 5, Figure 6 and Figure 8 show simulation results for a magnitude 6 event occurring on the southern segment of the Rhine River

Fault in terms of PGA and spectral acceleration (Sa) at 0.5 Hz, 1Hz, 2Hz, 5 Hz and 10 Hz as a function of the roughness parameter, rupture velocity and nucleation position respectively. On each of these figures, an example of simulated waveforms (East-West component of acceleration) is also shown to see clearly the effect of each considered source parameters. PGA and Sa are obtained as the geometrical mean of two quantities measured on the horizontal components. This choice is consistent with what is generally done for GMPEs and give us the possibility of a comparison with them.

We considered a large range of variation for each parameter to explore the effect on the ground motion. Several authors (e.g. Gallovic and Brokesova, 2004; Causse et al., 2009 and 2010) have given different probable values of roughness for the slip distribution ranging it between 0.7 and 1.6, we then let $\mathcal{K}$ vary uniformly between 0.3 and 2 to explore a wider range.

For v_r as well we selected a wide range letting it vary between 2100 *m/s* and 3400 *m/s*. For this latter parameter we assumed subshear rupture propagation on average with the maximum rupture velocity smaller than the average crustal shear wave speed of about 3500 *m/s*.

For the nucleation position, any location on the fault plane has been considered.

Simulations were first performed looking at the influence of one parameter at a time. In Figure 5**,** the influence of $\mathcal{K}$ on ground motion was investigated performing 100 simulations with a fixed $v_r = 2800m/s$ and the hypocenter location at the center of the fault. In Figure 6**,** we performed 100 simulations fixing $\mathcal{K}$=1 and the hypocenter location again at the center of the fault to check the impact of v_r. We observe a linear trend at low frequency and an exponential trend at high frequencies. Variability for specific values of the source parameters is inherited by the aleatory variability of the slip phases, which are randomly chosen in the k^{-2} model as discussed in the first section. We can also observe that, for high frequencies (above 5*Hz*), ground motion is not influenced by rupture velocity (the trend is linear with a slope close to

zero) up to a threshold above that we observe an exponential increase. This threshold is between 3000*m/s* and 3200*m/s*.

To simultaneously investigate the influence that these two parameters have on ground motion, in Figure 7 results of simulations obtained combining the variability of $\mathcal{K}$ and v_r are shown, while the nucleation position is always fixed at the center of the fault. The six subplots refer to six frequencies and, for each frequency, a clear trend of the ground motion parameters as a function of both the roughness and rupture velocity is observed. Specifically the dependency on the roughness looks quite linear at all the considered frequencies. From Figure 7 we observe how roughness and rupture velocity jointly affect the ground motion. We can see how amplitude variation for low frequencies (up to 2*Hz*) is of about two order of magnitude: we identified three different color areas (each color area corresponds to half order of magnitude), separated by black lines, for which the logarithm of the spectral acceleration and PGA is almost constant. If we move to higher frequencies, we observe a wider range of variation (with five different areas highlighted for the 10*Hz* plot). From this figure we can also conclude that for small value of $\mathcal{K}$ (below 0.5 for spectral acceleration and between 0.4 and 0.9 for PGA) ground motion amplitudes is less sensitive to rupture velocity. For larger values of $\mathcal{K}$, variations of v_r become really important to control the simulated ground motion values.

Concerning the variability associated with the nucleation position on the fault plane, we separated its variation along the strike and the dip directions, here represented by the variables x_n and y_n respectively. Figure 8 shows the ground motion parameters as extracted from the simulations as functions of the nucleation position on the fault plane. In this subset of simulations we fixed $v_r = 2800 m/s$ and $\mathcal{K}$=1. A correlation at very low frequencies (0.5 Hz) can be observed. Specifically we computed the corner frequency for the simulated events. Since they range between 0.1 and 0.5 Hz, we expect that the directivity effect is more important around this interval while it starts to disappear at higher frequencies (>=1 Hz). To investigate

this aspect we performed another set of simulations for a magnitude M_w 5.0 event. To be consistent with the new magnitude, also the size of the fault was reduced while the corner frequency of the synthetics increased at around 1.5 Hz. It is well known that the directivity effect is mainly observed in a range below the corner frequency (e.g. Causse et al., 2009). For this reason, in Figure S3 of the supplementary material**,** the results of the test for a M_w 5 event clearly show the rupture directivity effect up to 2 Hz.

This sensitivity analysis shows that both the rupture velocity and the roughness degree of the slip have a strong impact on the high frequency strong motion parameters while they generally control the amplitude of the ground motion. For this reason, constraining their range of variation could significantly reduce the epistemic variability of the simulated ground motion. We should take into account these results to build up a proper strategy of selection of realistic values for these parameters to not introduce strong biases in the calculation.

4.2. Fault geometry and Stress Drop

Another important aspect consists in evaluating the static stress drop associated to our simulations. This stress drop is related to the slip distributions and hence to the roughness parameter. It is independent from seismological data (but depends on geological information) and we can compare it with the estimates from the EGF reported in TABLE 1. According to Kanamori and Anderson (1975), for an extended fault, the static stress drop associated to a particular slip distribution can be defined as:

$$\Delta\sigma = C\mu\frac{\bar{S}}{\tilde{L}} \tag{7}$$

where C is a non-dimensional shape factor (≈1 in many cases), μ is the rigidity, $\bar{S}$ is the mean slip value over the fault plane and $\tilde{L}$ represents the length of the rupture area defined as the square root of the surface where the slip is over 20% of the maximum slip. The size of the

rupture area is correlated to the value of the roughness degree of the slip: for large values of $\mathcal{H}$ the slip is concentrated in small areas characterized by large amplitudes, inversely, for small values of $\mathcal{H}$, we will have large rupture area with lower amplitude.

The stress drop depends on selection for the fault geometry and different fault surfaces can lead to different stress drop values. Moreover, for the same fault surface, different rupture areas (different values of $\mathcal{H}$) corresponds to different stress drops. To better understand this aspect, in Figure 9 we show $\Delta\sigma$ as a function of $\mathcal{H}$ for three different fault geometries. For each case we performed 450 simulations linearly varying $\mathcal{H}$ and v_r with the same procedure as for the tests showed in Figure 7. The first test corresponds to the entire extension of the segment identified for the southern part of the Rhine River Fault, (27 km along strike and 16 km along the dip) (Figure 9a). For the other two cases, we reduced the fault area to 1/3 of the original one keeping the same shape ratio between *L* and *W* and considered two different fault position with respect to the surface: one is placed in depth while the other reaches the surface. As discussed by Causse et al. (2013), stress drop should increase with $\mathcal{H}$ for a fixed fault area. We observe in all the cases an almost linear increase of mean $\Delta\sigma$ value with the roughness. Also stress drop variability at fixed $\mathcal{H}$ comes from randomness of slip phases. Another intuitive result is that reducing the fault area the mean slip value increases producing larger stress drops (Figure 9b and c).

Strong motion peak parameters (PGA and PGV) are also shown in Figure 9 as functions of the mean stress drop value (computed for each $\mathcal{H}$) and rupture velocity. They are well correlated with the position of the fault with respect to the target site. Larger values of peak parameters are observed when reducing the fault size and increasing the stress drop, with a significant increase when the small fault is placed at shallow depth (Figure 9c).

Even if these analyses shown that stress drop variability associated to $\mathcal{H}$ is not large enough to better constrain roughness values (one order of magnitude of variation for $\mathcal{H}$ corresponds in

just one order of magnitude of variation for $\Delta\sigma$), it is important to note that stress drop values obtained using the entire fault surface inferred from geological knowledge are really small compared to the average stress drop computed from the EGF ($\sim 8MPa$). Since the EGF technique is based on the self-similarity assumption, we concluded that using a smaller fault surface could be more appropriate for our simulations. Geological faults are generally big structures, while rupture surface should be related to the characteristics of the event we want to simulate and can be just a portion of the geological fault plane. For the rest of the paper, all the simulations relative to a M_w 6 event will be performed for a smaller fault plane (the red rectangle in Figure 9b).

Finally, we can also observe that high values of rupture velocity result in very large peak amplitudes on the simulations.

4.3. Blind simulations

To perform blind simulations a useful strategy consists in defining the probability distribution of the source parameters to control their variability. An example is given in Figure 10 for the rupture velocity. For a uniformly distributed probability (between 2200 *m/s* and 3400 *m/s*), resulting values of PGA are between 10% and 60% of *g*. For a normal distribution centered in $v_r = 0.8v_s$ and truncated in the same interval as above, the resulting PGA variability is significantly reduced (from 10% to 38% of *g*). From this simple example we can easily deduce that constraining the variability in the source parameters with a proper probability distribution will reduce ground motion variability of our simulations.

For the roughness parameter, Causse et al. (2010) showed a correlation between its logarithm and the logarithm of the PGA. Under the far-field approximation, they show that $PGA \propto (\mathcal{K}/L)^{3/2}$ proposing a lognormal distribution for this parameter with a magnitude dependent mean value and a standard deviation $\sigma = 0.12$. Our results show an almost linear

increase of the PGA with $\mathcal{K}$ (Figure 5) probably due to the very near fault conditions. In any case, the dependence of the PGA from the roughness of the slip is confirmed and it is still reasonable to adopt a lognormal distribution. Nevertheless, mean value of this distribution is not clearly identified in literature. According to Gallovic & Brokesova (2004), a reasonable value of $\mathcal{K}$ must be chosen around 1, while using the hypothesis of self-similarity between the target event and the EGFs, Causse et al. (2009) found $\overline{\mathcal{K}} = 0.74$. The empirical relation derived by Causse et al. (2010) shows, for a M_w 6 event, $\overline{\mathcal{K}} = 1.6$. For this reason, we decided to perform three different sets of simulations changing the mean value for the distribution of the roughness parameter.

For the rupture velocity we selected a range of variation according to observations from source studies where v_r is generally found between 60% and 90% of v_s(e.g. Heaton, 1990). So we decided to assume a normal distribution with a mean value $\overline{v_r} = 0.8v_s = 2800m/s$ and $\sigma = 400m/s$, truncated between 2100*m/s* and 3400*m/s* to avoid super shear propagation.

According with results obtained by Mai et al. (2005), nucleation position should be chosen close to zones with significant slip values. Since our explored slip distributions mostly have large slip patches far from the fault edges, we chose normal distributions centered in the middle of the fault plane for x_n and y_n.

In Figure 11 are summarized all the chosen source parameters probability density functions (Figure 11a) and the choices we made for the roughness mean value, the fault size and its position with respect to the main fault plane (Figure 11b).

Finally we let vary all the source parameters together, according to the probability distributions described above, and performed three sets of 500 blind simulations for a magnitude 6 event located on the southern fault segment and we compared results with prediction of different

GMPEs. Each set has a different mean roughness value: 0.74 (from self-similarity assumption), 1.0 (from Gallovic & Brokesova 2004) and 1.6 (from empirical relations).

We chose four different prediction equations that were compatible with the considered case study: Boore and Atkinson (2008), Chiou and Youngs (2008), Cauzzi et al. (2014) and Akkar and Bommer (2010). Some details about the considered GMPEs are shown in TABLE 2. All these GMPEs take into account the soil site condition through the V_{S30} parameter (mean shear wave velocity in the first 30 m from the surface). For the selected site we assumed V_{S30} = 580 m/s (Chartier 2015).

As an example, in Figure 12 PGA and Sa (computed at 0.5, 1, 2, 5 and 10 Hz) values from simulations are compared with GMPEs predictions for a M_w 6 event recorded at BREM station. As observed also by other authors (e.g. Baumann and Dalguer, 2014; Dalguer and Mai, 2012), empirical models predictions generally produce higher values than simulation results in near source conditions (distances lower than 10 km). Here we observe the same discrepancy at all frequencies, except for the simulations obtained with a mean roughness value of $\overline{\mathfrak{K}} = 1.6$. This is clearly visible between 5 and 10 Hz, where we can observe a strong increase of the simulated ground motion values.

Figure 12 also shows simulation results for different ranges of rupture velocities: $v_r \leq 2400m/s$, $2400 < v_r < 3000m/s$ and $v_r \geq 3000m/s$. As expected, due to the choice of a normal distribution for rupture velocity centered on 2800*m/s*, most of the data are concentrated in the range between 2400 and 3000*m/s*.

Finally, we decided to adopt the roughness mean value that comes from the self-similarity assumption (0.74) in order to fix the stress drop of the target event as the average of the values computed for the EGFs. Under this assumption, the Figure 13 shows the results of three sets of 500 blind simulations obtained for three different scenarios: the first one considering only the

southern segment of the Rhine River Fault; the second one considering only the northern segment; the third one considering the two segments together.

In Figure 13 the spectral accelerations are shown as functions of the period T (obtained as the geometrical mean of the two horizontal components) in terms of mean and standard deviation for each scenario. Each single fault has been associated to a magnitude 6 event, such that a rupture scenario propagating through both the segments generates a M_w 6.5 event.

As we can see, if we consider the two faults separately, results are very similar with the northern segment producing larger amplitudes especially for periods between 0.05 and 0.1 s (10 to 20 Hz). Results obtained involving both the two fault segments are giving, as expected, larger amplitudes with values of response spectra over 1 g for periods between 0.1 s and 0.2 s (5 to 10 Hz).

The possibility to investigate different scenarios results extremely important in the case of a probabilistic hazard analysis. Including faulting models in PSHA let us to identify which could be the source contributing the most to the hazard (Chartier 2015).

Discussion and conclusions

In the framework of the BestPSHANI workshop (Best Practices in Physics-Based Fault Rupture Models for Seismic Hazard Assessment of Nuclear Installations, Vienna, Austria, 18–20 November 2015), whose purpose was to discuss the applicability of different ground motion simulation techniques for hazard assessment of nuclear installations, we propose a near fault application to the Upper Rhine Graben based on the multi empirical Green's function approach coupled to a k^{-2} kinematic source description. The importance of performing simulations relies on the fact that GMPEs are often not robust in near fault conditions. The lack in near fault records makes them not able to cover all the possible earthquake scenarios likely leading to incorrect ground motion estimation.

Numerical simulations can be a way to overcome this problem, although they need to be properly calibrated with the weight of each parameter investigated. One of the advantages of the approach we use for modeling the seismic wave propagation is that a very detailed description of the crustal medium is not required because it is replaced by a significant number of records of small earthquakes. In the case of the application shown here, the Upper Rhine Graben, a region located at the border between France and Germany which is characterized by a low to moderate seismic activity, finding enough records was part of the challenge. From a database of about 30 events recorded in the last 15 years, we were able to extract 5 events which satisfy strict quality criteria to be used as EGFs. Even if it worked out in this case, this is one limitation of our application. Indeed improvement of seismic networks for regions demanding seismic hazard assessment is required to increase the robustness of ground motion prediction.

After choosing the BREM station as the target site, we tested the influence of source parameters on the simulations. In particular we showed the correlations of the ground motion parameters with the roughness of the slip, the rupture velocity and the nucleation position. The roughness parameter mostly shows a linear correlation with ground motion amplitudes, while for the rupture velocity we observe a faster growth at high frequency (mimicking an exponential behavior). Nucleation position is related to rupture directivity effect and it has a strong influence only at low frequencies below the corner frequency of the simulated event. To better understand the physical meaning of the roughness parameter and try to reduce its range of variability, we studied its correlation with the static stress drop. All these parameters have shown to play a key role and we studied in details this effect to better constrain the variability of the ground motion and properly calibrate simulations.

While for rupture velocity and the hypocentral position we can make some assumptions on the most probable values and the associated variability, the roughness parameter has no *a priori* constraints because it is directly related to the slip distribution, which can be quite different

from earthquake to earthquake. So we decided to adopt a lognormal probability distribution for it according to Causse et al. (2010) and to explore three (very) different mean values as proposed in several previous studies (e.g. Causse et al., 2009; Gallovic and Brokesova, 2004). Without any *a priori* assumption, as discussed also by Del Gaudio et al. (2015), using the EGF approach, $\overline{\mathcal{K}} = 0.74$ should be preferred according to the self-similarity hypothesis.

We then performed blind simulations for a magnitude 6 event occurring on the southern segment of the Rhine River Fault system assuming *a priori* probability distributions of source parameters and comparing them with four different GMPEs. We found that generally our simulations lead to lower ground motion estimations (and variability) than the ones obtained from GMPEs, with a strong dependence on the input source parameters. This comparison is not straightforward though, because in both cases we are not comparing the same ground motions estimators. Regarding simulations, the level and the variability of the results are reflecting the large uncertainties on the controlling source parameters, exhibiting the lack of physical constrains on them. In the future, physics-based rupture models should help to reduce those uncertainties. Regarding the GMPEs, the results are reflecting the lack of near fault data and the summation of uncertainties due to both extrapolation and ergodicity. Large epistemic uncertainties remain in both methodologies, although they are essentially different for each. The relative consistency between GMPEs with respect to simulations may just be symptomatic of the common methodology of GMPEs which are essentially lacking of data in near source conditions, while the biases of simulations are essentially different and independent ones originating from the lack of physics.

With this work we confirm that, for a defined earthquake scenario, distance is not sufficient to explain the variability of the ground motion. In this synthetic case, it is dominated by the uncertainty on sources parameters (roughness degree, average rupture velocity, etc.) rather than on aleatory parameters such as slip distribution or hypocenter location. Our work clearly

identifies parameters controlling the ground motion, and subsequently point out which uncertainties should future studies aim at reducing. Meanwhile, those uncertainties should be taken into account in ground motion computations. This is an important point if the simulations carried out have to be included into a probabilistic seismic hazard model to complete information that comes from GMPEs at short distances from the fault. For a PSHA, it is necessary not only to retrieve the average ground motion produced by a given earthquake, but the distribution of all the possible scenarios that can be generated.

Finally, for the specific case study we also showed results for three different sets of scenarios considering the two selected segments of the Rhine River Fault. For each of them we showed average simulated ground motion and its variability in terms of acceleration response spectra as functions of the period of the oscillation. For these simulations we fixed the magnitude to M_w 6 for the case of a single fault involved in the rupture process, and M_w 6.5 when considering both the fault segments. Our results show that the northern segment produces on average larger amplitudes than the southern one, and that the worst case of a bigger earthquake producing over the two fault segments can reach high ground motion level for a target site located in very near fault conditions (more than 1 g for response spectra ~5 Hz with a PGA of 0.4 g). Again, this result is strongly dependent on the uncertainties we have on source parameters. In blind conditions, where no benchmark are available, source parameters should be accurately investigated and their natural variability properly reproduced. A strategy which combines physics-based simulation methods with the knowledge that comes from real observations could be in future the right choice to correctly calibrate source parameters and hence to obtain realistic strong ground motion predictions.

Acknowledgments

We thank LBRG and Stefan Stange in particular for providing the BREM station data that we used in the simulations, and the additional stations data needed to invert for moment tensors. We thank Sophie Lambotte and Cécile Doubre at EOST/Renass for their help getting the data. We warmly thank Hervé Jomard for his help plotting the BDFA map. This research activity was supported by the PIA ANR SINAPS@ project, grant no ANR-11-RSNR-0022.

References

Aki, K. & Richards, P.G., 2002. Quantitative Seismology, 2nd ed., University Science Books, Sausalito, CA.

Akkar S., Bommer J.J. (2010) Empirical equations for the prediction of PGA, PGV and spectral accelerations in Europe, the Mediterranean and the Middle East. Seismol Res Lett 81:195–206.

Aochi H., Durand V. and Douglas J. (2011), Influence of super-shear earthquake rupture models on simulated near-source ground motion from the 1999 Izmit (Turkey) earthquake Bull. Seism. Soc. Am. 101 726–741.

Baumann, C., and L. A. Dalguer (2014). Evaluating the compatibility of dynamic rupture-based synthetic ground motion with empirical ground-motion prediction equation, Bull. Seismol. Soc. Am. 104, no. 2, 634–652, doi: 10.1785/0120130077.

Bertrand, G., Elsass, P., Wirsing, G., Luz, A. (2006), Quaternary faulting in the Upper Rhine Graben revealed by high-resolution multi-channel reflection seismic. Compte Rendu Des Geosciences 338, 574–580.

Boore, D. M. (2001). Comparisons of ground motions from the 1999 Chi-Chi earthquake with empirical predictions largely based on data from California, Bull. Seism. Soc. Am. 91, 1212-1217.

Boore, D.M. and Atkinson, G.M. (2008) Ground-Motion Prediction Equations for the Average Horizontal Component of PGA, PGV, and 5%-Damped PSA at Spectral Periods between 0.01 s and 10.0 s. Earthquake Spectra: February 2008, Vol. 24, No. 1, pp. 99-138.

Brune, J.N. (1970), Tectonic stress and the spectra of seismic shear waves from earthquakes, J. geophys. Res., 75, 4997--5009.

Campbell, K. W., & Bozorgnia, Y. (2014). NGA-West2 ground motion model for the average horizontal components of PGA, PGV, and 5% damped linear acceleration response spectra. Earthquake Spectra, 30(3), 1087-1115.

Causse, M., Cotton, F. & Mai, P.M. (2010), Constraining the roughness degree of slip heterogeneity, J. Geophys. Res., 115, B05304.

Causse, M., Cotton, F., Cornou, C. & Bard, P. Y. (2008), Calibrating median and uncertainty estimates for a practical use of empirical Green's functions technique, Bull. Seism. Soc. Am., 98, 344--353.

Causse, M., Dalguer, L. A. and Mai, P. M. (2013), Variability of dynamic source parameters inferred from kinematic models of past earthquakes, Geophys. J. Int. doi:10.1093/gji/ggt478.

Causse, M., E. Chaljub, F. Cotton, C. Cornou & P.Y. Bard (2009), New approach for coupling k-2 and empirical Green's functions: Application to the blind prediction of broadband ground-motion in the Grenoble basin, Geophys. J. Int., 179 (3), 1627--1644.

Cauzzi C, Faccioli E, Vanini M, Bianchini A (2014), Updated predictive equations for broadband (0.01–10 s) horizontal response spectra and peak ground motions, based on a global dataset of digital acceleration records. Bull Earthq Eng 13:1587–1612. doi:10.1007/s10518-014-9685-y.

Chartier, T. (2015), Étude probabiliste de l'aléa sismique pour un site du Fossé Rhénan Supérieur. Master II final report, Tâche 1.2.2 du projet ANR SINAPS@.

Chiou, B.S.J. and Youngs, R.R. (2008), An NGA Model for the Average Horizontal Component of Peak Ground Motion and Response Spectra. Earthquake Spectra: February 2008, Vol. 24, No. 1, pp. 173-215.

Cultrera, G., Cirella, A., Spagnuolo, E., Herrero, A. & Pacor, F. (2010), Variability of kinematic parameters and its implication on the choice of the design scenario, Bull. Seism. Soc. Am., 100, 941--953.

Cuppillard, P., Delavaus, E., Burgos, G., Festa, G.,Vilotte, J.P., Capdeville, Y. & Montagner, J.P. (2012) RegSEM: a versatile code based on the spectral element method to compute seismic wave propagation at the regional scale, Geophys. J. Int., 188 (3), 1203--1220.

Dalguer, L. A., and P. M. Mai (2012), Prediction of near-source ground motion exceeding 1g at low frequencies (<2 Hz) from Mw∼6.5 deterministic physics-based dynamic rupture simulations, in Proc. of the 15th World Conference on Earthquake Engineering (15WCEE), Lisbon, Portugal, 24–28 September 2012.

Dalguer, L. A., and S. M. Day (2007), Staggered-grid split-node method for spontaneous rupture simulation, J. Geophys. Res. , 112, B02302, doi:10.1029/2006JB004467.

Day, S. M., L. A. Dalguer, N. Lapusta, and Y. Liu, (2005), Comparison of finite difference and boundary integral solutions to three-dimensional spontaneous rupture, J. Geophys. Res., Vol. 110, B12307, doi:10.1029/2005JB003813.

De Matteis, R., Convertito, C., Zollo, A. (2016), BISTROP: Bayesian Inversion of Spectral-Level Ratios and P-Wave Polarities for Focal Mechanism Determination. Seismol Res Lett 87 (4), DOI: 10.1785/0220150259.

Del Gaudio, S., Causse, M. & Festa, G., 2015, Broad-band strong motion simulations coupling k-square kinematic source models with empirical Green's functions: the 2009 L'Aquila earthquake. Geophysical Journal International 203 (1): 720-736. doi: 10.1093/gji/ggv325.

Donahue, J. & Abrahamson, N., (2014) Simulation-Based Hanging Wall Effects. Earthquake Spectra: August 2014, Vol. 30, No. 3, pp. 1269-1284.

Douglas, J. (2016),Comment on the paper 'A risk-mitigation approach to the management of induced seismicity' by J. J. Bommer, H. Crowley and R. Pinho. Journal of Seismology, Volume 20, Issue 1, pp 393-394.

Douglas, J., Edwards, B. (2016), Recent and future developments in earthquake ground motion estimation, Earth-Science Reviews, Volume 160, Pages 203-219, ISSN 0012-8252.

Dumbser, M. & Käser, M. (2007), An arbitrary high-order discontinuous Galerkin method for elastic waves on unstructured meshes – II. The three-dimensional isotropic case. Geophys. J. Int. 171 (3): 1324. doi: 10.1111/j.1365-246X.2007.03388.x.

Ferry, M., Meghraoui, M., Delouis, B. and Giardini, D., 2005. Evidence for Holocene palaeoseismicity along the Basel—Reinach active normal fault (Switzerland): a seismic source for the 1356 earthquake in the Upper Rhine graben. Geophys. J. Int. 160 (2): 554-572 doi:10.1111/j.1365-246X.2005.02404.x.

Gallovic, F. & Brokesova, J., 2004. On strong ground motion synthesis with the k−2 slip distribution, J. Seism., 8, 211--224.

Hartzell, S., Harmsen, S., Frankel, A. & Larsen, S., 1999. Calculation of broadband time histories of ground motion: Comparison of methods and validation using strong-ground motion from the 1994 Northridge earthquake. Bull. Seism. Soc. Am., 89, 1484--1504.

Hartzell, S.H. (1978), Earthquakes aftershocks as Green's functions, Geophys. Res. Lett., 5, 1--4.

Heaton, T. H. (1990), Evidence for and implications of self-healing pulses of slip in earthquake rupture, Physics of the Earth and Planetary Interiors, Volume 64, Issue 1, Pages 1-20, ISSN 0031-9201.

Herrero, A. & Bernard, P. (1996), Modeling directivity of heterogeneous earthquake ruptures, Bull. seism. Soc. Am., 86,4, 1149--1160.

Homuth, B., Rümpkera, G., Deckertb, H., Krachtc, M. (2014), Seismicity of the northern Upper Rhine Graben — Constraints on the present-day stress field from focal mechanisms. Tectonophysics, Volume 632, 29 September 2014, Pages 8–20.

Hutchings, L. (1994), Kinematic earthquake models and synthesized ground motion using empirical Green's functions, Bull. Seism. Soc. Am., 84, 1028--1050.

Irikura, K. & Kamae, K. (1994), Estimation of strong ground motion in broad-frequency band based on a seismic source scaling model and an empirical Green's function technique, Ann. Geophys., 37, 6.

Irikura, K. (1983), Semi-empirical estimation of strong ground motions during large earthquakes, Prev. Res. Inst. Kyoto Univ., **33**, 63–104.

Irikura, K. (1984), Prediction of strong ground motions using observed seismograms from small events, Proc. 8th World Conf. on Earthq. Eng., vol. 2, 465-472.

Irikura, K., 1986. Prediction of strong acceleration motion using empirical Green's functions, Procedings of seventh Japan earthquake engineering symposium, 151—156.

Lambert J., Winter T., Dewez T.J.B., Sabourault P. (2005). New hypotheses on the maximum damage area of the 1356 Basel earthquake (Switzerland). Quaternary Science Reviews, 24, pp. 381–399.

Kanamori H., Anderson D.L. (1975) Theoretical basis of some empirical relations in seismology. Bulletin of the Seismological Society of America 65:1073–1095.

Koketsu, K. & Miyake, H., 2008. A seismological overview of long period ground motion, J. Seismol., 12, 133--143.

Komatitsch, D., Liu, Q., Tromp, J., Süss, P., Stidham C., Shaw, J. H. (2004), Simulations of ground motion in the Los Angeles basin based upon the spectral-element method, Bull. Seism. Soc. Am., vol. 94, p 187-206.

Lancieri, M., Madariaga, R., & Bonilla, F. (2012). Spectral scaling of the aftershocks of the Tocopilla 2007 earthquake in northern Chile. Geophysical Journal International, 189(1), 469-480.

Mai, P.M., Spudich, P. & Boatwright, J. (2005). Hypocenter locations in finite-source rupture models, Bull. seism. Soc. Am., 95, 965--980.

Matrullo E., Satriano C., Ibourichene A., Lyon-Caen H., Bernard P., Deschamps A., 2014. Scaling of earthquakes source parameters in Corinth rift (Greece) from spectral analysis: influence of attenuation and site effect. Second European Conference on Earthquake Engeneering and Seismology (2ECEES), Istanbul, Turkey, 24-29 August 2014.

Mayer-Rosa and Cadiot, 1979. A review of the 1356 Basel earthquake: Basic data. Tectonophysics, Volume 53, Issues 3–4, 20 March 1979, Pages 325-333.

Mazzieri, I., M. Stupazzini, R. Guidotti, and C. Smerzini (2013), Speed: Spectral elements in elastodynamics with discontinuous galerkin: a non-conforming approach for 3d multi-scale problems: International Journal for Numerical Methods in Engineering, 95, 991–1010.

Meghraoui, M., Delouis, B., Ferry, M., Giardini, D., Huggenberger, P., Spottke, I., Granet, M., 2001. Active normal faulting in the Upper Rhine Graben and Paleoseismic identification of the 1356 Basel earthquake. Science 293, 2070–2073.

Meyer, B., Lacassin, R., Brulhet, J., Mouroux, B., 1994. The Basel 1356 earthquake: which fault produced it? Terra Nova, 6-1, Blackwell Publishing Ltd, 1365-3121. DOI 10.1111/j.1365-3121.1994.tb00633.x.

Nivière B, Bruestle A, Bertrand G, Carretier S, Behrmann J, Gourry JC (2008) Active tectonics of the southeastern Upper Rhine Graben, Freiburg area (Germany). Quat Sci Rev 27:541–555.

Palumbo L., Baize S., Cushing M., Jomard H., David C., 2013. Devising BDFA: a new active fault database conceived behind nuclear safety assessment in France. 4th International INQUA Meeting on Paleoseismology, Active Tectonics and Archeoseismology (PATA), Aachen (Germany).

Song S., Dalguer L.A., and Mai P.M. (2014). Pseudo-dynamic source modeling with 1-point and 2-point staistcs of earthquake source parameters, Geophys. J. Int., 196, 1770-1786.

Schmedes J, Archuleta RJ, Lavalleé D (2010) Correlation of earthquake source parameters inferred from dynamic rupture simulations. J Geophys Res 115:B03304.

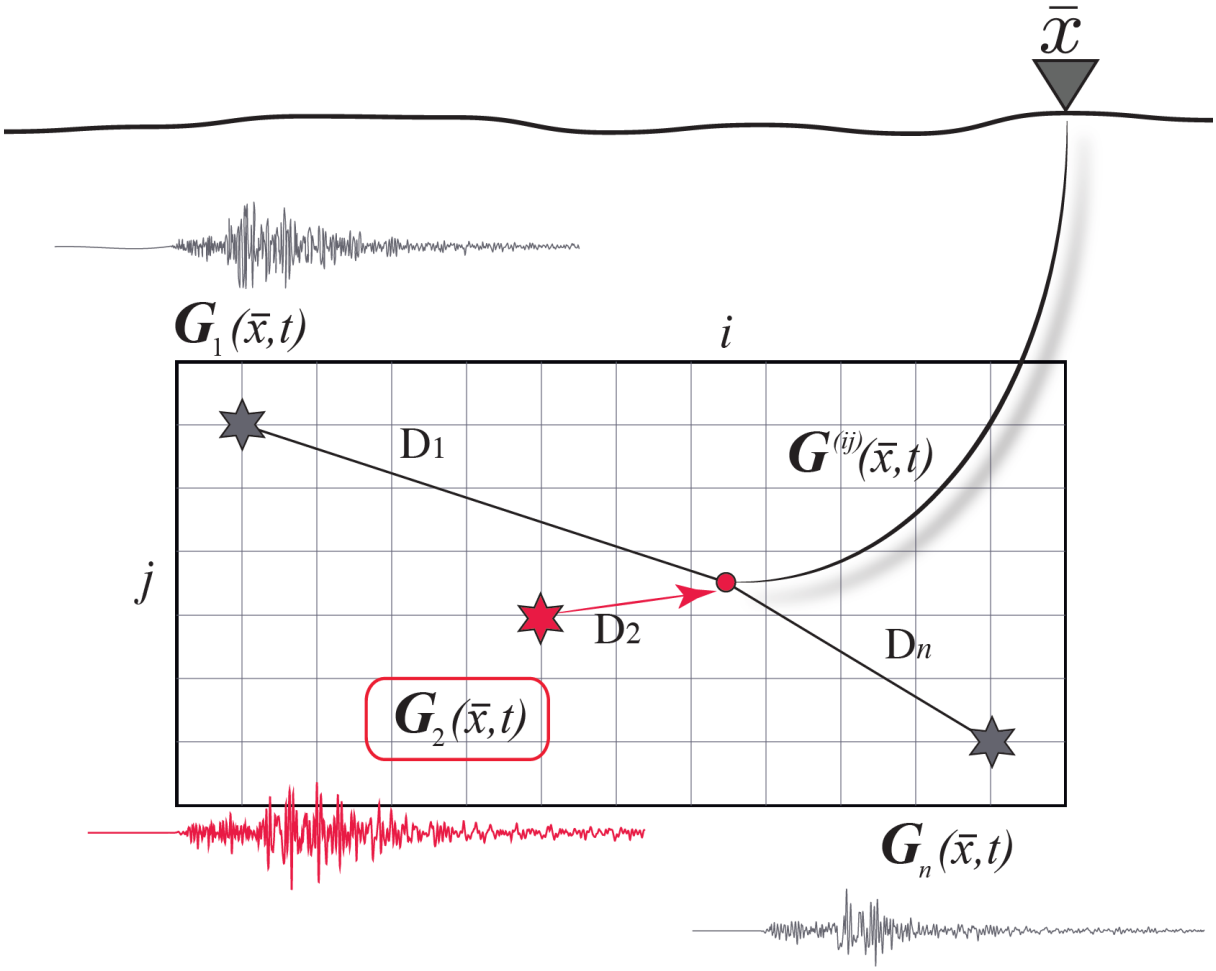

Figure 1 Schematic view of multi-EGF technique. Stars locate *n* different small earthquakes recorded at station *x*, that are candidate for being the EGF used at each point of the gridded fault. To determine which of the *n* different EGF is applied at each grid point, distance D_1, D_2, … D_n are calculated. At the red spot, D_2 is found to be the shortest distance. The EGF for this point is $\boldsymbol{G_2(\bar{x},t)}$.

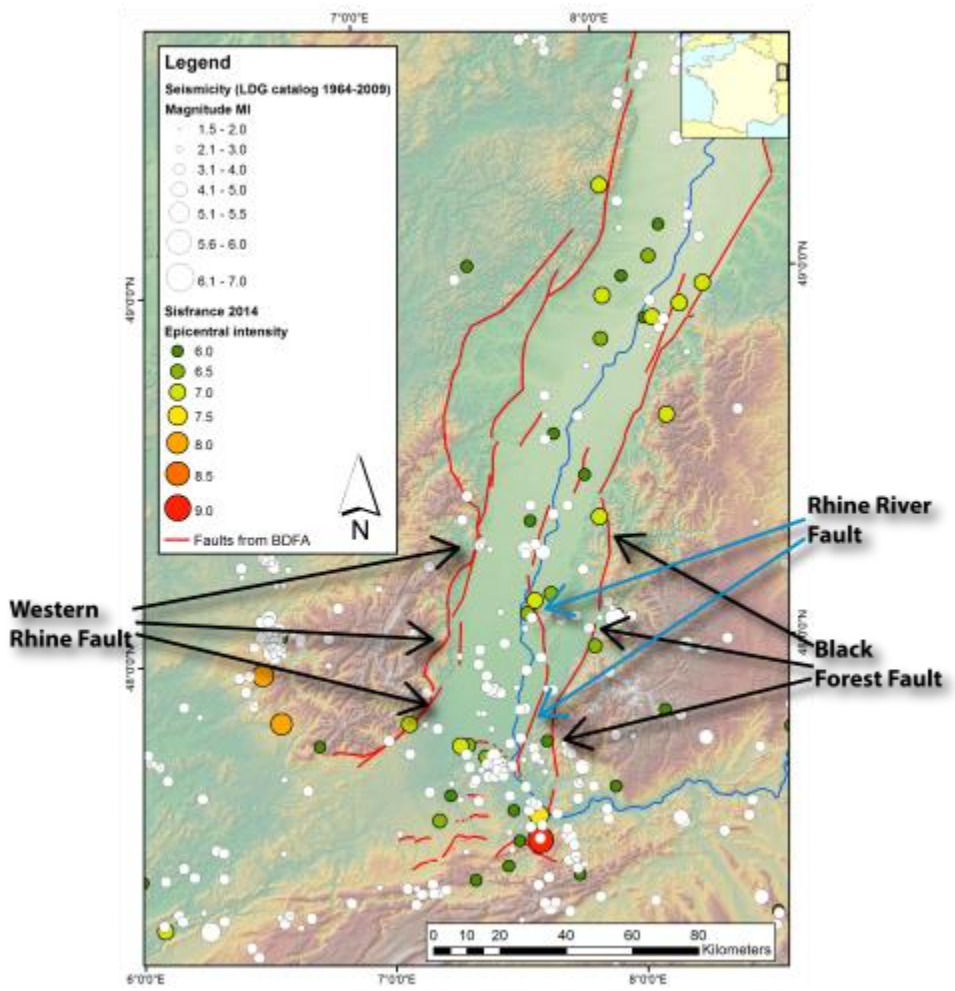

Figure 2 Seismicity and faults map of the Upper Rhine Graben; in particular the Western Rhine Fault and the Black Forest Fault systems are highlighted, which follow the borders of the Graben, and the Rhine River Fault, which follows the river path. As indicated in the upper legend, white circles represents recorded earthquakes in the area (from 1964 to 2009), while colored circles represents historical earthquakes in the area (different colors refers to different estimated intensities).

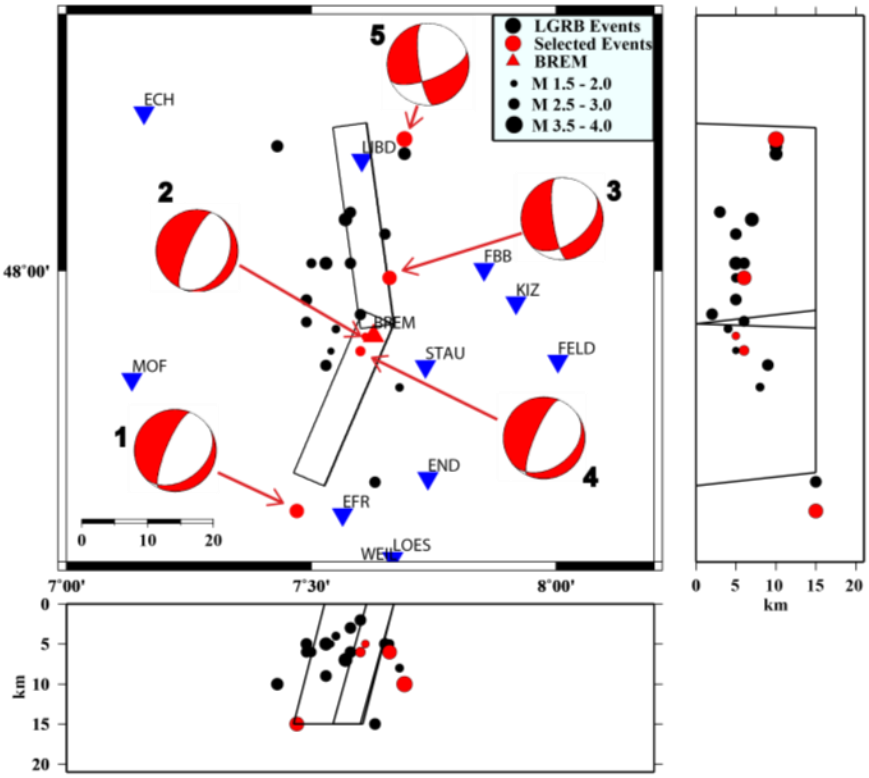

Figure 3 Simplified map of the area, showing the location of the considered events (black dots with a magnitude dependent size) and the surface projection of the modelled faults. Red dots represent the selected EGFs (identification numbers are the same as Table 1) for which focal mechanism solutions (computed fixing the strike and the dip angle, according to the hypothesis made for the considered fault geometry, and retrieving the rake angle from eq. 5) are also plotted on the map. The French and German stations located in the area are represented with blue triangles. Bottom and right panels are vertical sections in the EW and NS directions respectively.

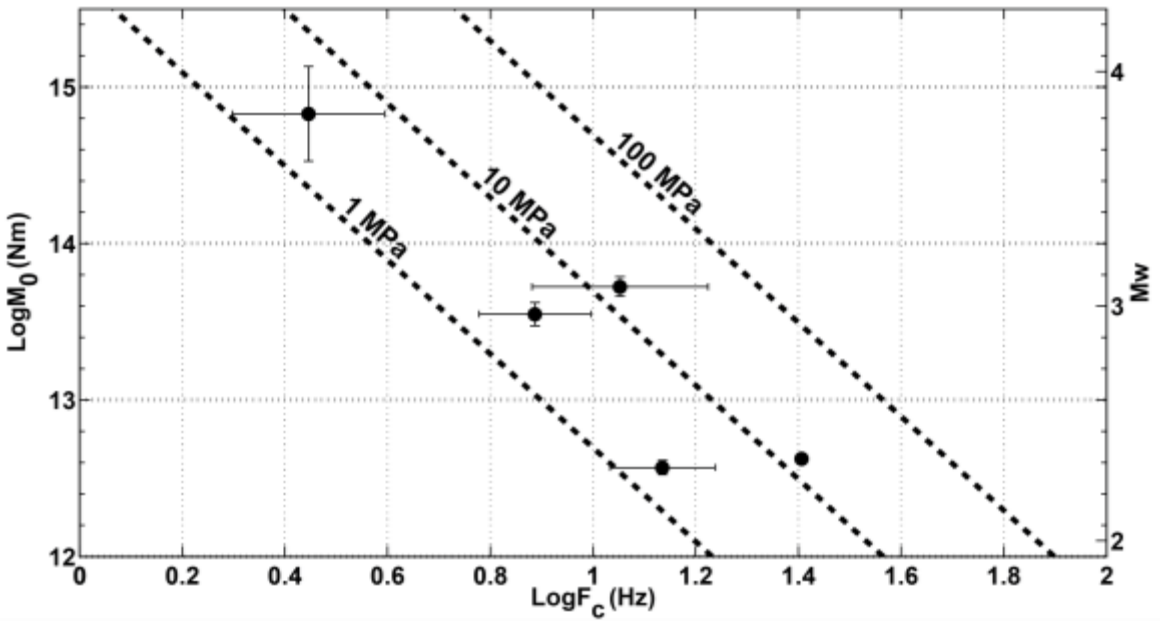

Figure 2 Logarithm of the corner frequency as a function of the logarithm of the seismic moment. Dashed lines represent constant stress drop values of 1, 10 and 100 MPa. Error bars represent the standard deviation associated to the different estimates of corner frequency and seismic moment from different stations.

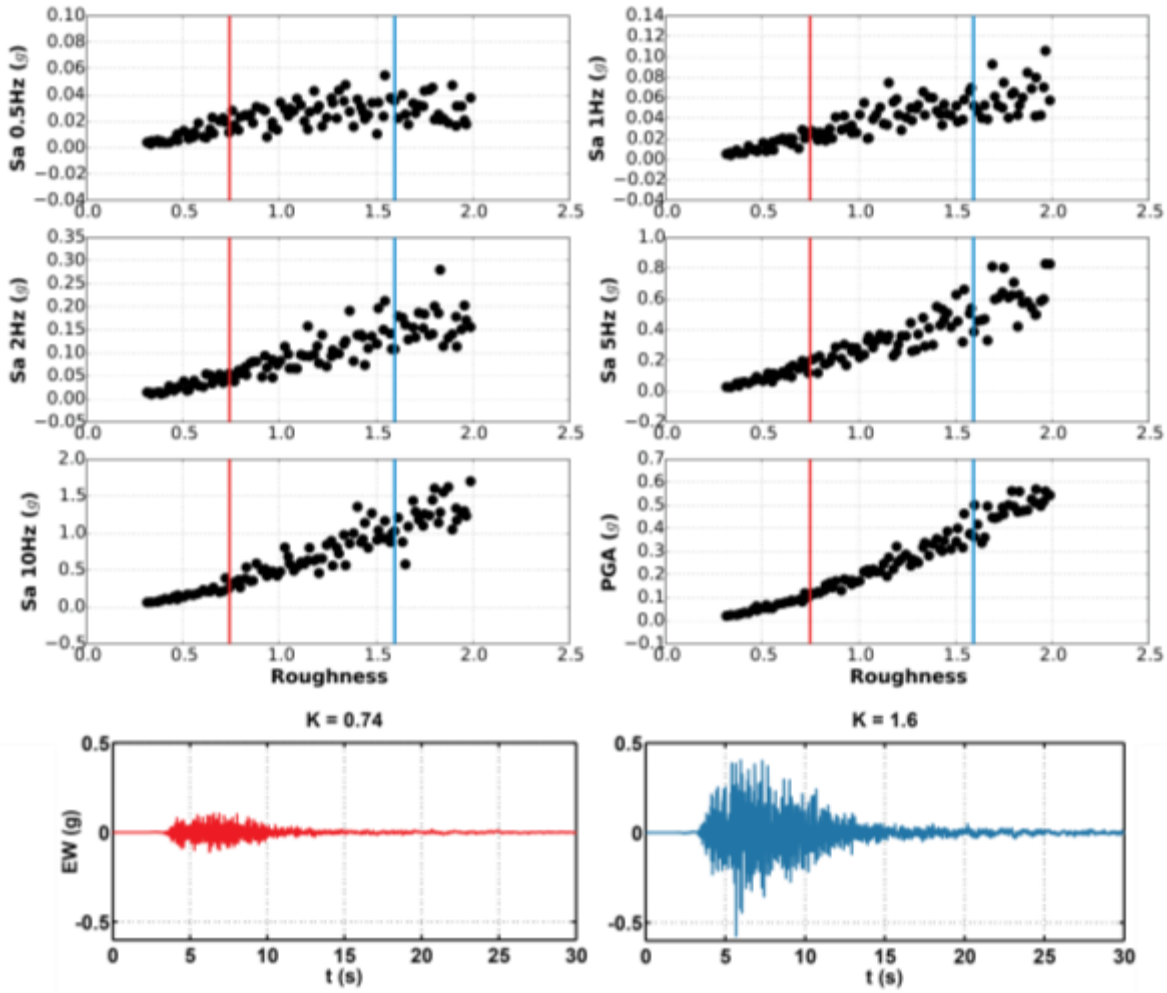

Figure 3 Spectral acceleration at 0.5 Hz, 1 Hz, 2 Hz, 5 Hz, 10 Hz and PGA as functions of the roughness parameter for a M_w 6 event occurring on the southern segment of the Rhine River fault. The nucleation position is fixed at the center of the fault and the rupture velocity is fixed to 2800 m/s. Red and blue lines on the plots corresponds to two values of the roughness parameter, 0.74 and 1.6, for which an example of simulated waveforms is shown.

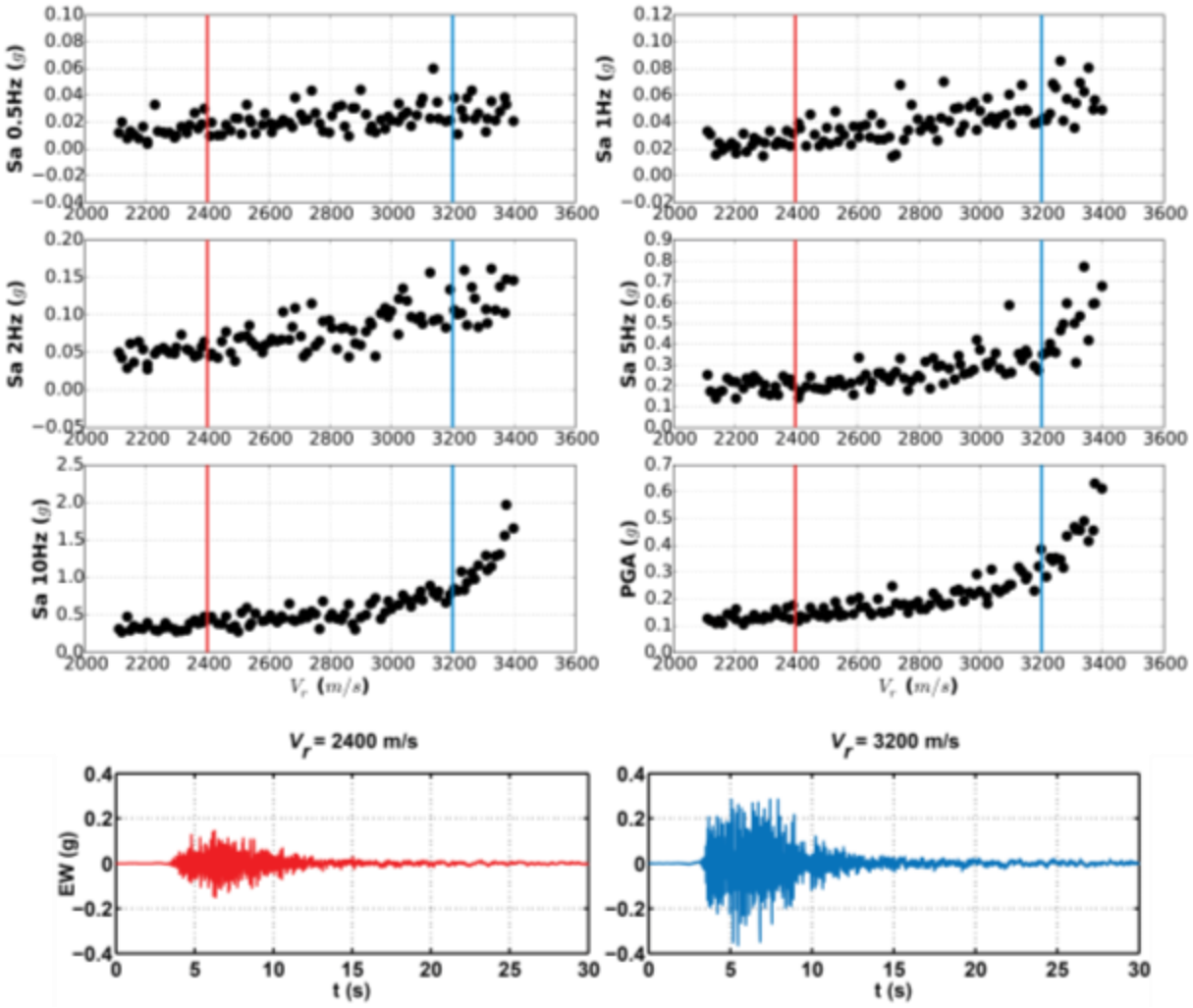

Figure 4 Spectral acceleration at the same frequencies as in Figure 5 and PGA as functions of the rupture velocity for a M_w 6 event occurring on the southern segment of the Rhine River fault. The roughness parameter is fixed to 1 and the nucleation position is fixed at the center of the fault. Red and blue lines on the plots corresponds to two values of rupture velocity, 2400 and 3200 m/s, for which an example of simulated waveforms is shown.

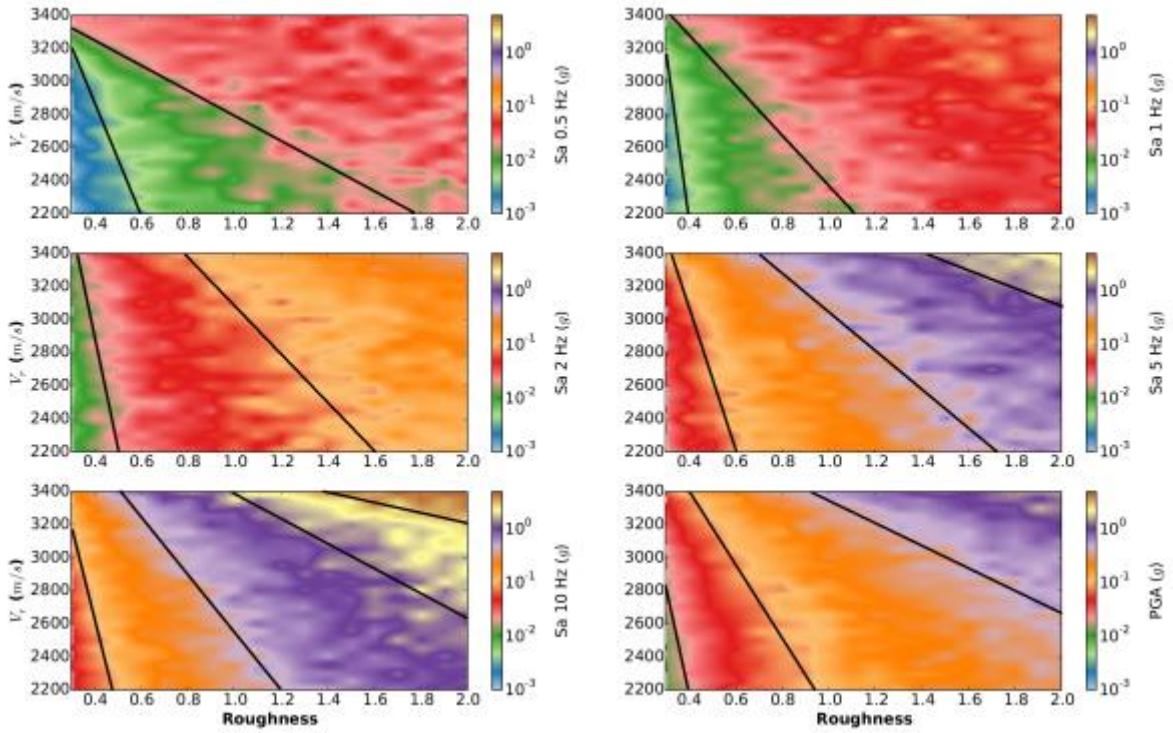

Figure 5 Spectral acceleration in logarithmic scale at same frequency as in Figure 5 and PGA as functions of the rupture velocity and the roughness parameter for a M_w 6 event occurring on the southern segment of the Rhine River fault. Only the nucleation position is fixed at the center of the fault. Paired color scale is used to highlight ground motion variations. Black lines separate qualitatively zones in which amplitudes are almost constant.

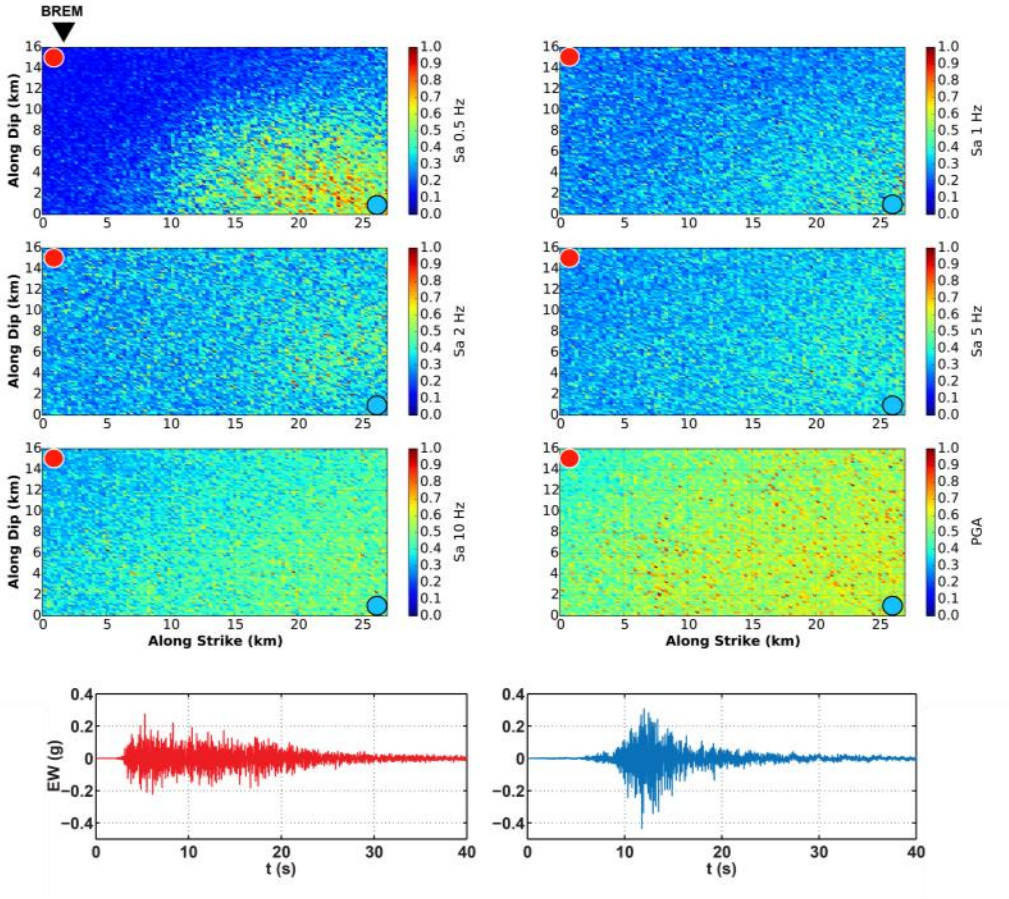

Figure 6 Normalized spectral acceleration and PGA as functions of the nucleation position for a M_w 6 event occurring on the southern segment of the Rhine River fault. Each point in a plot corresponds to a specific location for the rupture initiation points. The roughness parameter is fixed to 1 and the rupture velocity to 2800 m/s. The location of the target station with respect to the fault surface trace is also indicated. Red and blue spots on the plots corresponds respectively to an anti-directive and directive positions for which an example of simulated waveforms is shown.

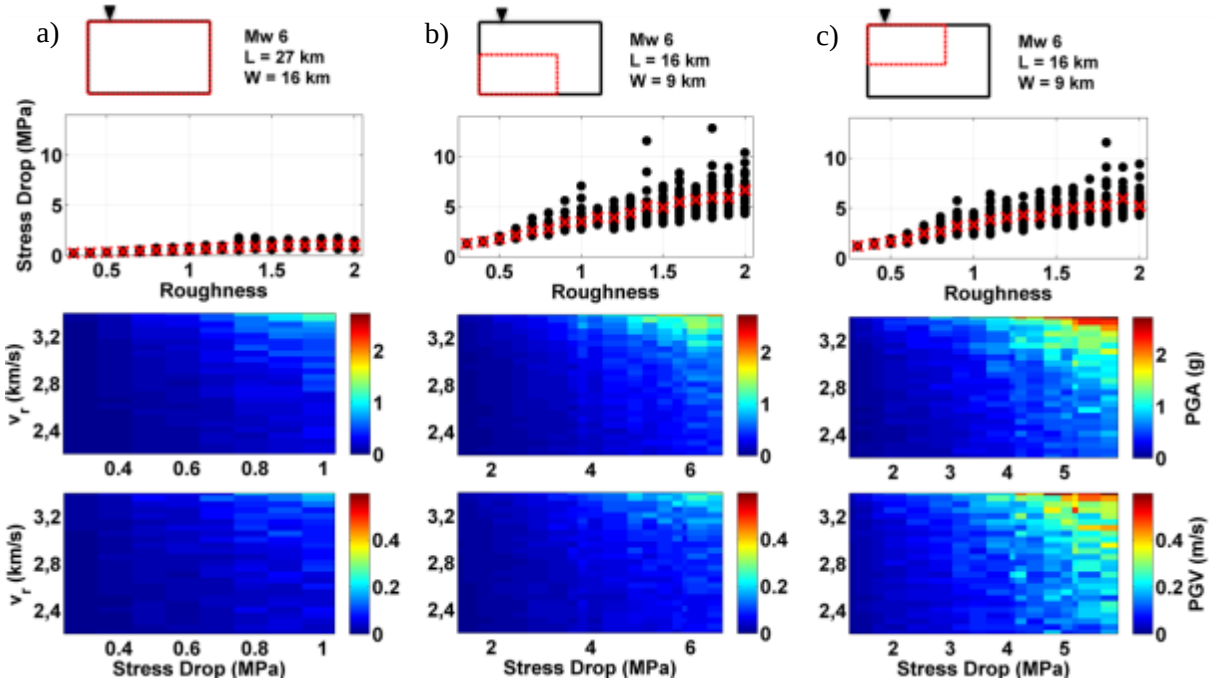

Figure 9 Top panels : Stress drop as a function of the roughness parameter (red crosses represent average values for fixed K) for the three different fault geometries a) Southern segment of the Rhine River fault; b) smaller fault surface with the same shape ratio of a); c) same fault of b) but placed at a shallow depth. In the bottom panels PGA and PGV distributions are shown as functions of mean $\Delta\sigma$ and v_r values for the same cases.

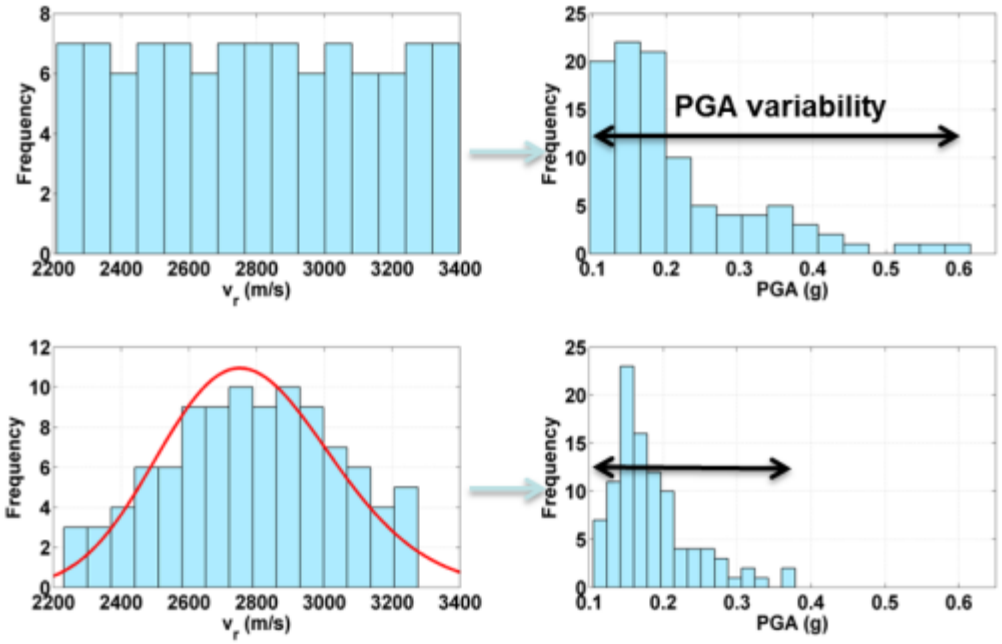

Figure 10 Influence of source parameters variability on the resulting ground motion. On the top: A uniform distribution of rupture velocity with resulting PGA distribution; on the bottom, normal distribution of v_r centered in $v_r = 0.8v_s$ and truncated between 2200 m/s and 3400 m/s with resulting PGA distribution.

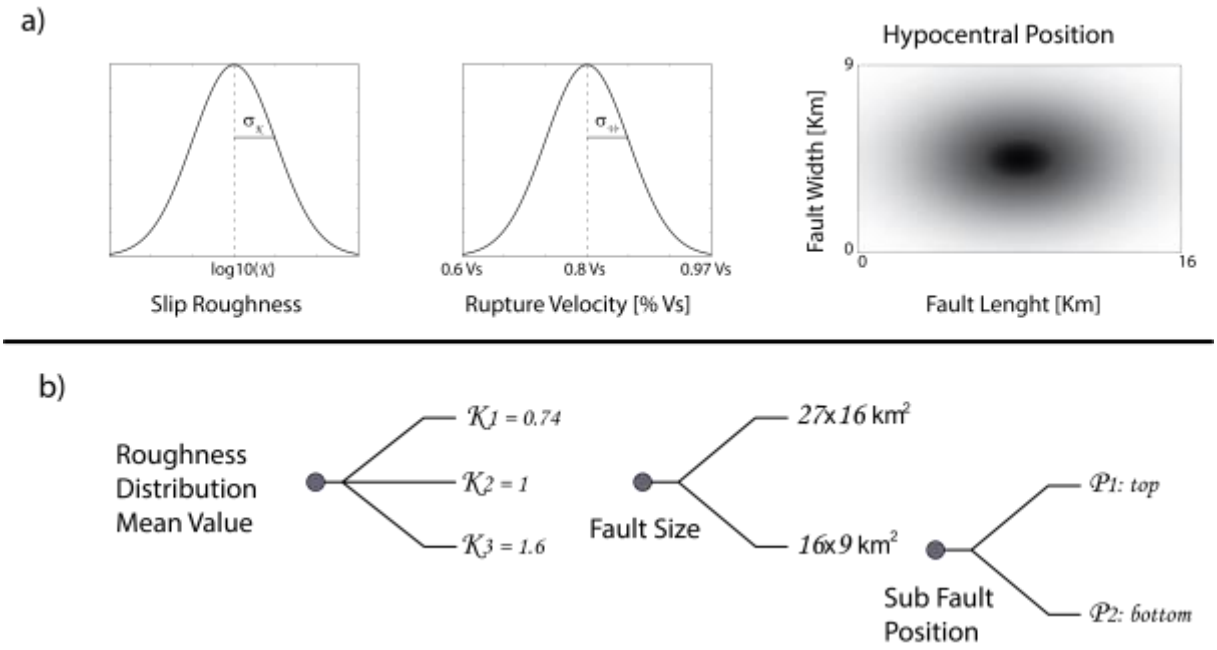

Figure 11 Considered probability density functions for the roughness parameter, the rupture velocity and the hypocentral position on the fault (a). Hypothesis made for blind simulations are also shown (b): mean values for the roughness parameter, considered fault size and its relative position with respect to the main fault plane.

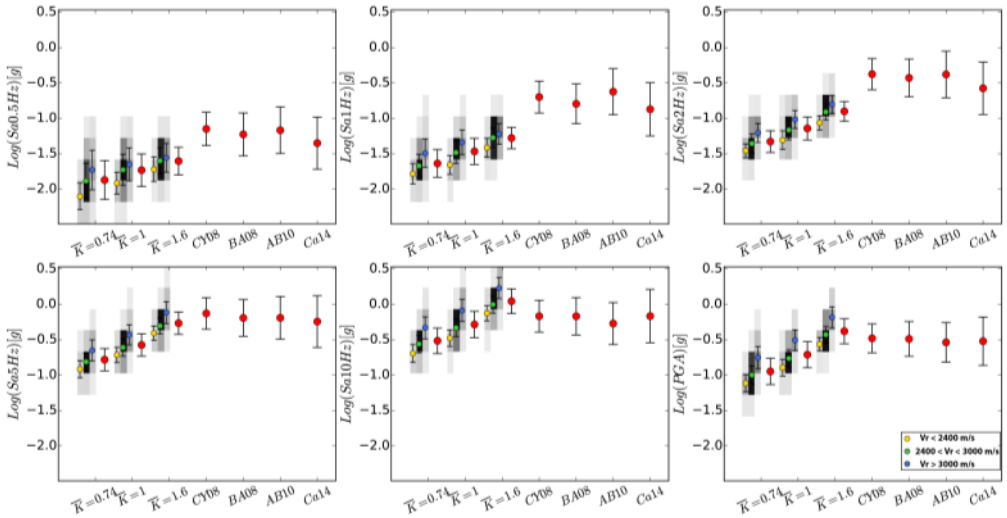

Figure 12 Comparison between simulations and GMPEs in terms of PGA and Sa (0.5, 1, 2, 5 and 10 Hz) for a M_w 6 event recorded at BREM station. Red dots represent the mean values for simulations (with different mean values of roughness parameter distribution) and GMPEs; error bars represent one σ interval. For simulations we also show density of values (in grey scale), mean and standard deviation for different ranges of rupture velocity.

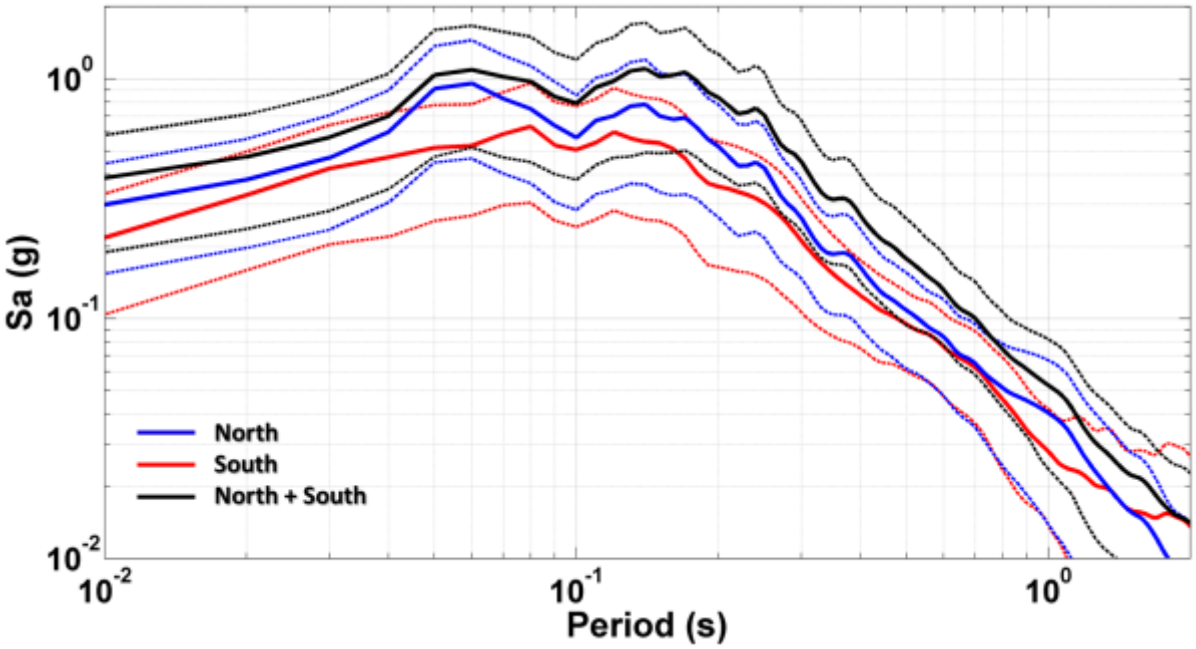

Figure 13 Spectral acceleration versus period of an equivalent harmonic oscillator with 5% damping for three different earthquake scenarios (only southern segment in red, only northern segment in blue and both the segment together in black). Solid lines represent the average of 500 simulations, while dashed lines represent the ± 1 σ interval.

TABLE 1 Source parameters for the selected EGFs: location from LGRB; moment magnitude, corner frequency and stress drop calculated as the average of the estimations at each station. Standard deviations for magnitude, corner frequency and stress drop are also indicated. For EGF 2 standard deviations are not indicated because only one record is available.

EGF #	Date	Time	M_w	σ_{Mw}	Lat (°)	Lon (°)	Depth (km)	f_c (Hz)	σ_{fc}	$\Delta\sigma$ (MPa)	$\sigma_{\Delta\sigma}$
1	26/09/2002	21:01:40.30	3.0	0.2	47.67	7.47	15	8	2	3	1
2	18/05/2005	15:34:10.10	2.3	-	47.91	7.61	5	25	-	15	-
3	25/07/2005	01:36:32.00	3.1	0.2	47.99	7.66	6	11	4	35	40
4	15/12/2009	21:12:35.00	2.3	0.1	47.89	7.60	6	14	3	3	2
5	01/11/2011	19:22:16.00	3.8	0.7	48.18	7.69	10	3	1	7	7

TABLE 2 GMPEs used for the comparison.

Reference Paper	Validity range of distance	Validity range of magnitude	Used metric	Origin of used data
Boore and Atkinson (2008)	1 – 200 km	5 – 8	R_{JB}	California and Taiwan.
Chiou and Youngs (2008)	1 – 200 km	4 – 8.5	R_{JB}, R_{RUP}	Tectonic region all over the world (subduction earthquakes are excluded).
Cauzzi et al. (2014)	1 – 150 km	4.5 – 7.9	R_{RUP}	Europe, Japan, California, China, New Zealand and Taiwan (subduction earthquakes are excluded).
Akkar and Bommer (2010)	5 – 100 km	5 – 7.6	R_{JB}	Europe and Middle East.